



Phase-sensitive seeded modulation instability in passive fiber resonators

Florent Bessin^{1,2}, Corentin Naveau¹, Matteo Conforti¹, Alexandre Kudlinski¹, Pascal Szriftgiser¹ ¹ & Arnaud Mussot¹ [✉]

Modulation instability is one of the most ubiquitous phenomena in physics. Here we investigate the phase-sensitive properties of modulation instability with harmonic seeding in passive fiber resonators. Theoretical investigations based on the Lugiato–Lefever equation with time dependent pump and a three-wave truncation show that the dynamics of the system is sensitive to the relative phase between input signal, idler, and pump waves. The modulation instability gain can even vanish for a peculiar value of the initial relative phase. An advanced multi-heterodyne measurement technique had been developed to record the real time evolution, round-trip to round-trip, of the power and phase of the output cavity field to confirm these theoretical predictions.

¹Univ. Lille, CNRS, UMR 8523-PhLAM Physique des Lasers Atomes et Molécules, Lille F-59000, France. ²Aston Institute of Photonics Technologies, Aston University, Birmingham B4 7ET, UK. ✉email: arnaud.mussot@univ-lille.fr

In dispersive and weakly nonlinear systems, a continuous wave (CW) may be unstable with respect to small perturbations. This phenomenon, known as modulation instability (MI) leads to the amplification of low frequency disturbances at the expense of the strong CW¹. MI has been widely investigated in optical fibers, where long interaction lengths are allowed by their extremely low losses². Besides the spontaneous MI, where the initial perturbation is noise, parametric amplification (or seeded MI) takes place when a signal is injected together with the pump. In this case, huge amplification gains (70 dB) over large bandwidths (120 nm) had been reported^{3,4}. Furthermore, potentially noiseless amplification can be achieved when signal and idler waves with symmetric frequency shifts with respect to the pump are launched *simultaneously* at the fiber input. In this configuration, the parametric gain depends on the relative phase of the input waves (phase-sensitive amplifiers^{3,5}), giving rise to so called squeezed photon states. These properties make phase-sensitive amplification of great interest for high bit rate modern telecommunication systems⁶.

Recently, MI has been widely investigated in dissipative systems such as microresonators because nonlinear effects are strongly enhanced due to their huge quality factors. Moreover, through appropriate conditions, MI is a fundamental triggering process to generate optical frequency combs (OFCs), the rulers of light, which revolutionized the science of ultra-precise measurements^{7,8}. As weak powers are required to reach the cavity MI threshold, most of the work has been performed with CW pump lasers. However, while weak, the optical power is high enough to induce thermal drifts of the microresonator characteristics which imposes an active stabilization technique⁷. This issue was resolved by driving the resonator with pulsed pumps⁹, thus avoiding the use of complex electronics to compensate for thermal effects. This recent evolution allowed for the generation of ultra-stable OFCs for astrometric measurements¹⁰ or of low-timing jitter ultrashort optical pulses through nonlinear filtering¹¹, to name a few applications.

Pulsed pumping configurations impose a strict match between the repetition rate of the pump pulse train and the free spectral range of the resonator. The pump spectrum is composed of several discrete components separated by (a multiple of) the free spectral range of the cavity⁹. When the pump is modulated, its spectrum is composed by only a few comb lines, which can experience different detunings with respect to the closest cavity resonances. The dynamics associated with this multi-line pumping scheme involve multiple four-wave mixing processes and is rather complex. In the context of MI,

investigations involving pulsed or modulated pumps were limited to simple specific configurations such as bi-chromatic pumping schemes^{12–16} or tri-chromatic ones, with identical powers¹⁷. However, in the first case, none of these studies investigate the sensitivity of the intra-cavity field to the relative phase between input components, and in the second case, it focuses on the sensitivity of the idler and signal generated by four-wave mixing to the relative phase between the three pumps. Note that what is referred to as parametric seeding of passive cavities in the literature is related to the generation of many additional inner-bands within the input pump spectrum due to multiple four-wave mixing processes^{18,19}, thus not to the basic phase sensitive process.

In this paper, we investigate the phase sensitivity of the modulation instability process in passive resonators driven by a weakly modulated pump (a strong pump and two weak symmetric sidebands). Given the dissipative nature of the system, after an initial transient due to MI, the optical field may reach a stationary, periodic solution (an OFC). This OFC may be interpreted as an attractor of the infinite-dimensional system describing the optical evolution inside the cavity²⁰. We show theoretically and experimentally that the output amplitude and relative phase depends on the relative input phase, making the attractor position to move over all the phase plane.

Results and discussion

Theory. In order to model passive cavities driven by a three-wave input, we use the Lugiato–Lefever equation (LLE²¹) accounting for time-dependent pump^{12,22} (see “Methods”). The driving field is composed of three waves, the carrier wave, the signal, and idler waves, frequency shifted by the same amount from the pump. We investigate the dynamics of this system by expanding the intra-cavity electric field by considering these three Fourier modes^{23,24} (see Supplementary Notes 1). The respective cavity detuning of the carrier and signal/idler waves is defined (from the closest resonances) $\delta_p = \delta_0$, $\delta_{i/s} = \delta_0 - 2l\pi \pm \beta_1\Omega L$ with $l = \arg[\min_l |\delta_0 + 2l\pi \pm \beta_1\Omega L|]$, respectively. This definition of signal/idler detuning can be easily interpreted by looking at the sketch reported in Fig. 1. The black lines in Fig. 1a depict the linear cavity transmission function and the red, green, and blue vertical dashed lines the linear phase accumulated by the signal, pump, and idler components over one round-trip, respectively. Note that typical lengths of fiber cavities are tens of meters, which give birth to several thousands of modes between the pump and signal/idler components, those ones being separated by a few megahertz typically. Thus, Fig. 1a is a simplified sketch not drawn with a realistic scale.

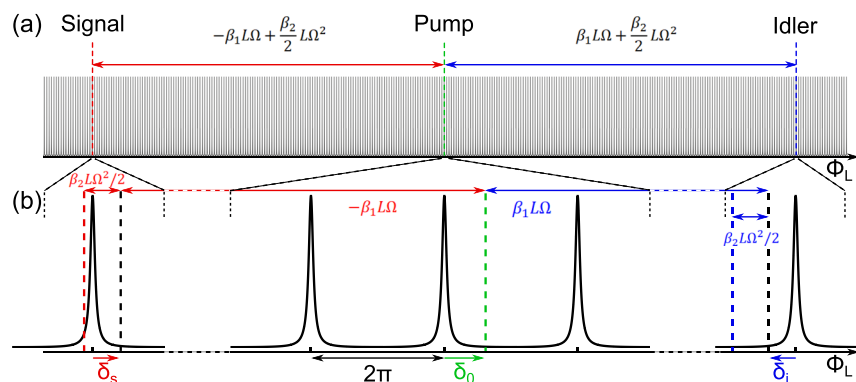


Fig. 1 Cavity resonances and pump/signal/idler locations. **a** Linear resonances of the cavity and cavity pumping configuration. **b** Zoom on the closest resonances from the pump, signal and idler waves. β_1 is the inverse of the group velocity, β_2 the group velocity dispersion expressed at the pump frequency, L the cavity length, Ω the pump signal pulsation shift, $\delta_{s,0,i}$ the signal, pump and idler detunings respectively, from the closest resonance and Φ_L the phase accumulated over one round-trip.

In this work, we limit our investigations to cavities pumped far away from their zero dispersion wavelengths where the first and second order dispersion terms are enough to capture the whole dynamics of the MI process. Consequently, we find that the linear phase difference between the pump and idler/signal (of angular frequencies $\omega_f = \omega_{i/s}$, respectively) are given by $[\beta_2 \Omega^2/2 \pm \beta_1 \Omega]L$ (where $\Omega = |\omega_{i/s} - \omega_0|$), respectively as can be seen in Fig. 1a and more precisely in the zoom in Fig. 1b.

There is a vast pumping configuration zoology depending on each wave's power, phase, and detunings that is too complex to be addressed analytically on the whole. In order to derive simple analytical expressions to predict the dynamics of the system, we focus on the following configuration where: (i) $\beta_1 \Omega L = 2m\pi$ ($m \in \mathbb{Z}$), therefore $\delta_0 = \delta_i = \delta_s$, (ii) the regime is monostable ($\delta_0/\alpha < \sqrt{3}$ ²⁵), (iii) the input signal and idler have equal amplitudes and phases ($P_{s,in} = P_{i,in}$ and $\phi_{s,in} = \phi_{i,in}$, which also entails $\phi_s = \phi_i$ and $P_s = P_i$), and (iv) signal and idler powers are much weaker than the pump one ($P_{0,in} \gg P_{i/s,in}$). While specific, this configuration corresponds to usual experimental setups. Approximated pump, signal, and idler stationary solutions can be found from the TWM (Eq. S4 in the Supplementary Note 1) following the method described in^{25,26}. We found that for each value of relative input phase $\Delta\xi = \phi_{s,in} - \phi_{0,in}$, two steady-state solutions exist. One of them is stable and corresponds to an attractor, while the other is unstable and corresponds to a saddle point²⁷. These solutions are depicted in Fig. 2a using the plane ($P_s, \phi_s - \phi_0$) in polar coordinates. Each value of $\Delta\xi$ can be identified by a color indexed in the legend in Fig. 2. We observe that by changing the relative input phase value $\Delta\xi$ from 0 to 2π , the steady-states form an aircraft propeller in the phase plane. Stable steady-states (thin solid line) are located mainly around the “blades”, while unstable saddle points (dashed line), mainly close to the rotor (see the zoom in Fig. 2b). Some examples of trajectories are shown in dash-dotted lines in Fig. 2a, b calculated

from the TWM (Eq. S4 in the Supplementary Note 1). We note that their final states marked with colored dots match perfectly with the predicted stable steady-states. Numerical simulations from the LLE Eq. 4 are depicted in Fig. 2c using a similar representation and scale than in Fig. 2a. The system converges toward attractors (marked by colored dots), whose positions match well with theoretical predictions depicted in Fig. 2a, thus confirming the validity of the three wave truncation. Note that trajectories bifurcate either to one “blade” or to the other, depending on the relative input phase value $\Delta\xi$. The change of direction takes place close to two specific values ($\Delta\xi \approx 1.95\pi$ and 0.95π). These correspond to two saddle points of the system marked by black circles in Fig. 2a–c that can be asymptotically reached for these specific values of $\Delta\xi$. Note that for these specific initial conditions (marked by orange circles in Fig. 2a–c), trajectories remain located very close to the rotor meaning that the system experiences the lowest gain. Thus, we can assume that signal and idler powers remain weak compared to the pump power ($P_0 \gg P_s$). Consequently, we can linearize the TWM (Eq. S4 in the Supplementary Note 1) around these values and derive the input phase value $\Delta\xi$ leading to minimum gain. We found the following expression (see Supplementary Note 1 for details):

$$\Delta\xi = \phi_{s,in} - \phi_{0,in} = -\arctan\left(\frac{\delta_0 - \gamma L P_0^{ss}}{\alpha}\right) - \frac{\pi}{4} + m\pi \quad (1)$$

m integer, for which the idler and signal converge asymptotically toward a saddle point that satisfies the phase relation:

$$2\phi_s^{ss} - 2\phi_0^{ss} = -\frac{\pi}{2} + 2m\pi \quad (2)$$

and power:

$$P_s^{ss} = \frac{\theta^2 P_{s,in}}{(\alpha + \gamma P_0^{ss} L)^2} \quad (3)$$

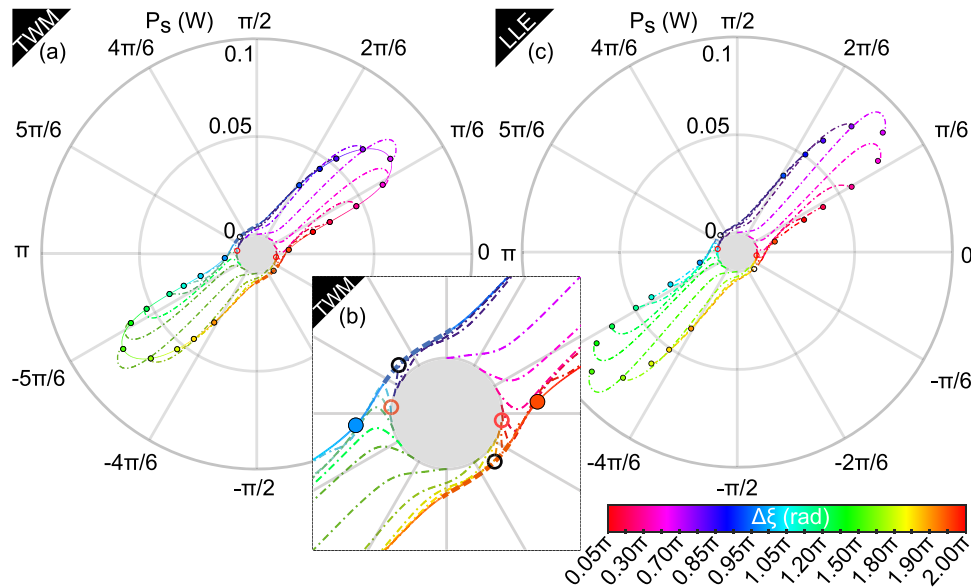


Fig. 2 Dynamic evolution in a phase plane. **a** Steady-states predicted from three wave mixing theory (TWM, see Supplementary Note 1) in the phase plane (P_s (Signal power), $\phi_s - \phi_0$ (pump-signal signal phase difference)). Solid colored lines and dashed colored lines stand for the stable and unstable steady-states, respectively. Thin dash-dotted curves correspond to trajectories calculated from TWM (Eq. S4 in the Supplementary Note 1) for $\Delta\xi$ (relative input phase) ranging from 0 to 2π . **b** Zoom around the origin of **(a)**. The orange circles in **(a, b)** denote the initial states corresponding to the specific input phases leading asymptotically towards the saddle points marked by the black circles (Eqs. 2 and 3). **c** Example of trajectories calculated from numerical simulations of the Lugiato Lefever equation (LLE, Eq. 4). In all cases, colored dots stand for the final states. Parameters: δ_0 (pump cavity detuning) = 0.05 rad, α (cavity loss) = 0.14, L (cavity length) = 169 m, γ (nonlinear coefficient) = $1.2 \text{ W}^{-1} \cdot \text{km}^{-1}$, P_{in} (pump power) = 0.2 W, β_2 (group velocity dispersion) = $-20 \text{ ps}^2 \cdot \text{km}^{-1}$, $P_{i/s,in}$ (input idler and signal power) = $1.10^{-2} \times P_{0,in}$, f_T (pump signal frequency shift) = $\pm \Omega_T/(2\pi) = \pm 59 \text{ GHz}$. The origin has been expanded ($P_s = 0$, gray zone) in order to improve the visualization.

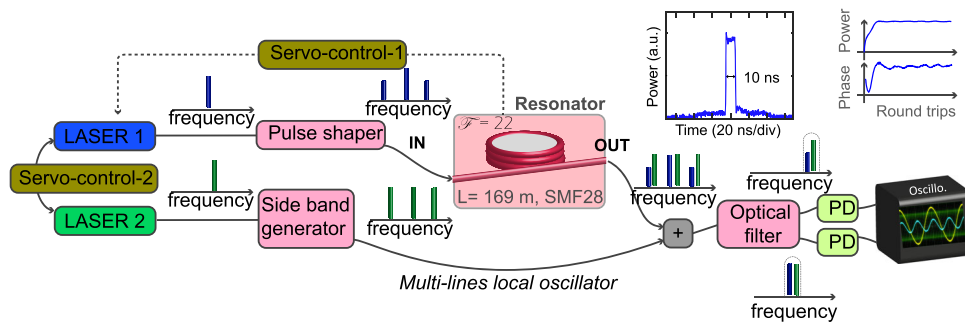


Fig. 3 Experimental setup. Simplified sketch of the experimental setup. A multi-heterodyne system, inspired from³⁴, had been implemented to trigger and analyze the modulation instability effect and to analyze the output cavity field in real time (see top right examples of power and phase evolutions). We launched 10 ns pulses (see central panel) to avoid stimulated Brillouin scattering. F: Finesse, L: cavity length, SMF: single mode fiber 28, div: division, PD: photo-detector, and Oscillo: oscilloscope.

Note that Eq. 2 corresponds exactly to the relation between input phase of idler, signal, and pump in the case of parametric de-amplification^{3,4,24,28,29} in single pass configurations.

Experiments. A simplified sketch of the experimental setup is depicted in Fig. 3. The cavity is made from a standard single mode fiber (SMF-28) closed by a 90/10 coupler leading to a cavity finesse of 22. Other parameters are similar to those used in the theoretical study and listed in Fig. 2 caption. The cavity is driven by a train of 10 ns square-shaped pulses to mitigate stimulated-Brillouin scattering³⁰ (see inset in Fig. 3) whose repetition rate is carefully adjusted to match with the free spectral range of the cavity. The pump is surrounded by two weak phase locked symmetric sidebands whose amplitude and phase are controlled with a complex optical filter. Furthermore, laser 1 is locked to the cavity by means of a servo-control system as in refs.^{31–33} to make it drifting with the cavity. The detection setup is inspired from the heterodyne optical time domain reflector developed in ref.³⁴ to monitor the longitudinal evolution of phase and intensity of Kerr combs in optical fibers. Here, the multi-line local oscillator is provided by an intensity modulated laser (laser 2, see Fig. 3a), which is phase locked with laser 1 with another servo-control system. We finally get the evolution in phase and intensity, round-trip to round-trip of the pump, signal, and idler waves by isolating their respective beatings with their closest local oscillator laser line with a highly selective optical filter (Fig. 3). We set the system in the configuration investigated analytically and numerically in Section 2.1 (see Fig. 2 caption). We used an input power $P_{0,in} = 0.20$ W ($P_0^{ss} = 0.71$ W), just above the MI cavity threshold. The frequency corresponding to the maximum of the MI gain bands was detected by recording the MI spectra triggered by noise when no signal/idler are launched within the cavity together with the pump. We found that maxima of MI bands were located at $f_T = \Omega_T/(2\pi) = \pm 54$ GHz in good agreement with theoretical predictions giving $f_T = \pm 59$ GHz (see spectra in Fig. S1d in Supplementary Note 1). In a second step, we tuned the seed frequency at this value and we increased their power up to 20 dB below the pump one (see the red spectrum in Fig. S1d in the Supplementary Note 1). By coherently seeding the MI process thinner spectral lines can be observed in the output spectrum as well as the birth of harmonics ± 108 GHz. The detuning of signal and idler waves was carefully tuned such that $\delta_i = \delta_s = \delta_0$ by following a method described in detail in the Supplementary Note 1. Finally, we recorded the signal/pump power and signal/pump relative phase evolutions as a function of the input pump-signal relative phase $\Delta\xi$. Two typical examples

are depicted in Fig. 4. In the first case, $\Delta\xi = 1.2\pi$ rad (blue curves) and the second one, $\Delta\xi = 0.05\pi$ rad (red curves). Figure 4a shows the power evolution. In both cases the pump and signal increase rapidly before reaching a stationary state at about 35 round-trips for $\Delta\xi = 1.2\pi$ rad (blue curves) and 80 for $\Delta\xi = 0.05\pi$ rad (red curves), respectively. Gain experienced by signal and idler waves differs on these two examples by a few dB. This fact illustrates one of the peculiar features of phase-sensitive parametric processes, for which amplification gain depends on the relative initial phase. The agreement between experiments (solid lines) and numerical simulations from the LLE (Eq. 4, in dashed lines) is very good with discrepancies of the decibel order over more than 30/40 dB gain between the first and last round-trip. The transient and steady stages are very well reproduced by our experimental measurements. Figure 4b shows the evolution of the relative phase between the pump and signal. These phase are measured with an uncertainty of 0.13 rad corresponding to the maximum phase accumulated by the system during the first round-trip, which is not measurable with our setup. Hence, we approximate the phase measured at the first round-trip to the input phase $\Delta\xi$. As observed for the signal power, the transient regime of the phase depends on $\Delta\xi$. It evolves from the initial value $\Delta\xi$ and reaches a stationary regime at about the same number of round-trips than for the signal power evolution. It is worth to point out the excellent stability of our measurement system since once the steady state is reached we get power and phase fluctuations lower than ± 0.4 dB and ± 0.09 rad, respectively (Fig. 4a, b). We limit the round-trip number to 210 in Fig. 4 in order to display both transient and stationary regimes of the process, but we were able to perform stable recordings over thousands of round-trips. The transient regimes are in very good agreement with numerical simulations from the LLE Eq. 4. We note that the experimental measurements of the relative intra-cavity phase are shifted by approximately 0.3π rad compared to numerical simulations. This discrepancy might originate from the condition $\beta_1\Omega L = 2m\pi$ ($m \in \mathbb{Z}$) (for which $\delta_0 = \delta_i = \delta_s$) that is not perfectly fulfilled in experiments. We estimated that an uncertainty of only a few kilohertz on the laser frequency ($\approx 0.1\%$ of the cavity-free spectral range and $5 \times 10^{-10}\%$ of the laser frequency) is enough to induce a shift of the relative intra-cavity phase of ≈ 6 mrad per round-trip.

By means of our experimental system, it is possible to plot the evolution of the signal characteristics (relative phase and intensity) in a phase plane ($P_s, \phi_s - \phi_0$) to highlight the formation of attractors that characterize the evolution of modulational instability in dissipative systems³⁵. The phase plane is depicted in Fig. 4c for the same values of $\Delta\xi$ considered in Fig. 4a, b. The

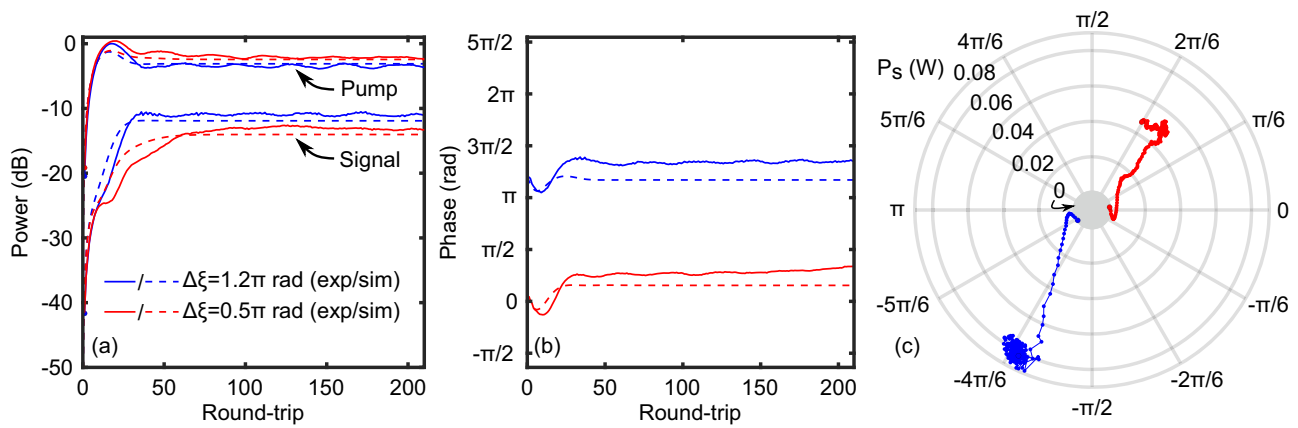


Fig. 4 Phase and intensity evolutions round-trip to round-trip. **a** Intra-cavity power of signal and pump wave versus the number of round-trip. **b** Relative intra-cavity phase between pump and signal versus the number of round-trip. **c** Phase plane (P_s (signal power), $\phi_s - \phi_0$ (pump-signal signal phase difference)). The solid and the dashed lines stand for the experiments and numerical simulations of the Lugiato–Lefever equation Eq. 4, respectively. Exp : experiments, Sim. : simulation and $\Delta\xi$ (relative input phase).

trajectories spiral toward attractors whose coordinates depend on the initial relative phase value, as expected from the theory³⁵. All these observations highlight the phase-sensitive nature of seeded MI in passive resonators. We also recorded the dependence of the signal and pump power on $\Delta\xi$ in order to evidence the existence of a particular value of relative input phase where the MI gain vanishes. We report in Fig. 5 the signal and pump power versus $\Delta\xi$ for different cavity round-trip numbers ($n = 25, 50, 75$, and 210). Experimental results appear in gray symbols (circles and squares for signal and pump, respectively) while numerical predictions in red and blue solid lines, respectively. Both pump and signal power are π -periodic and out of phase due to the energy exchange that flows from the pump wave toward sidebands components and vice-versa. A minimum (maximum) for the signal (pump) power is observed at $\Delta\xi = 0.95\pi$ and $\Delta\xi = 1.95\pi$. The experimental results are in good agreement with numerical simulations of the LLE Eq. 4 depicted in Fig. 5a, d in solid lines. We can notice that the agreement is worse around the minima for large round-trip numbers. In this case, the “width” of the curves obtained from numerical simulations decreases, in good agreement with experiments for $n = 25$ and $n = 50$ (Fig. 5a, b), while it is not possible to distinguish this narrowing from experimental recordings for a larger round-trip number (Fig. 5c, d). It would have required more recordings around this minimum value to be able to resolve these sharper transitions, which were not achievable in our system. Anyway, our experimental setup permitted to clearly observe the lowering of the gain for specific initial phase values as well as the shrinking of the gain curve for large round-trip number. The position of the gain minima is in good agreement with the theoretical predictions from Eq. 1 (vertical black dotted lines in Fig. 5).

We report in Fig. 6 the relative intra-cavity phase between the signal and the pump ($\phi_s - \phi_0$) versus the input pump-signal relative phase $\Delta\xi$. The green, blue, black, and red circles stand for the relative phase $\phi_s - \phi_0$ after $n = 25, 50, 75$, and 210 round-trips, respectively. We observe that the relative intra-cavity phase jumps of roughly 0.6π rad at the phase predicted by Eq. 1 (marked by black dotted lines). The amplitudes of these phase jumps are in qualitatively good agreement with the numerical simulations of the LLE Eq. 4 depicted in Fig. 6 by solid curves keeping the same color code. Note that we observed similar behaviors in the monostable regime for other cavity detuning values.

Conclusion

We investigated the phase-sensitivity of the modulation instability process in passive resonators when signal, idler, and pump waves are launched together at the cavity input. We developed specific theoretical tools to account for the dynamics of the process based on a truncated three wave model. We demonstrated that the gain experienced by the weak seed launched at the resonator input depends on the input relative phase between pump, signal, and idler waves. This phase sensitivity property leads the attractor to move in the phase plane. We found that for peculiar input phase values the gain vanishes. This is similar to what occurs in phase-sensitive amplifiers in simple propagation⁵. However, in the dissipative system considered here, the output relative phase is locked to a fixed value.

The theoretical predictions have been confirmed by experimental measurements based on a multi-heterodyne detection technique³⁴. It allowed us to monitor the round-trip to round-trip phase and power evolution of the intra-cavity pump and signal waves, until a stationary state is reached. The dynamical monitoring of an attractor formation requires highly accurate phase measurements and an excellent cavity stabilization over hundreds of round-trips. We faced this challenge to obtain a pretty good agreement with theoretical predictions. These first results achieved just above the cavity threshold pave the way to the observation of more complex nonlinear regimes such as spatio-temporal chaos^{20,36}, for which the knowledge of the electric field (phase and intensity) in real time would be a strong added value to get a better understanding of these phenomena. As an example, numerical simulations of our fiber cavity predict, as suggested in the seminal work of Halterman and co-workers²⁰, that Lorenz chaotic behavior³⁷ can be triggered above a critical detuning threshold where the cavity operate in bistable regime. Such an example is depicted in Fig. 7 for a normalized pump detuning of $\Delta = 3$, an input pump power of $P_{0,in} = 0.7$ W ($P_0^{ss} = 2.5$ W) and $\Delta\xi = 0$ rad. This configuration corresponds to the red dot on the upper-branch of the bistable cycle depicted in Fig. 7. As can be seen from the phase plan ($P_s, \phi_s - \phi_0$) depicted in Fig. 7b, the system does no longer converges to an attractor but follows an unpredictable trajectory that oscillates between two attractors. Hence, through this numerical example, we anticipate this experimental system might contribute to get a deeper understanding of complex nonlinear dynamics of resonators operating in chaotic regimes.

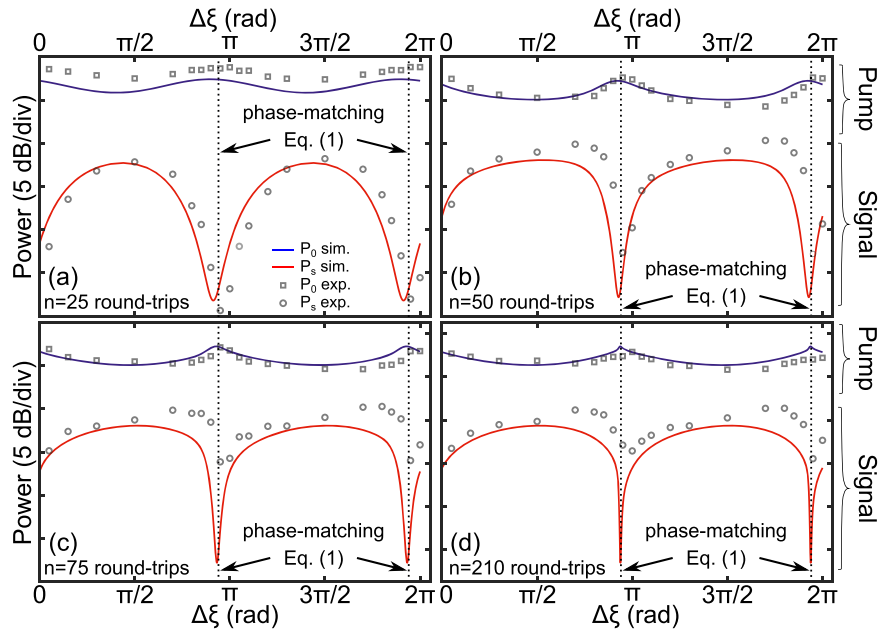


Fig. 5 Intra-cavity power evolution. a–d Intra-cavity signal and pump powers versus $\Delta\xi$ (relative input phase) at $n = 25, 50, 75$, and 210 round-trips, respectively. Gray circles and squares stand for the measured signal and pump power, respectively. Solid red and blue curves correspond to numerical simulations of the Lugiato–Lefever equation (Eq. 4).

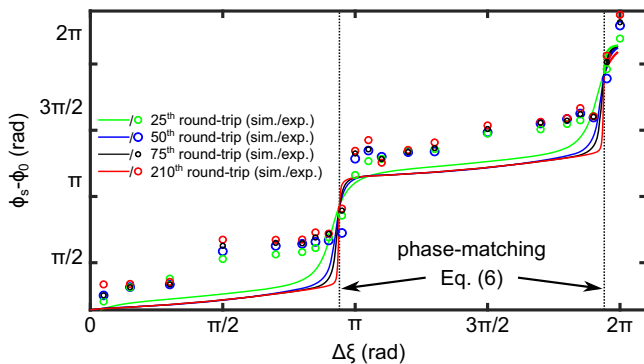


Fig. 6 Output phase evolution. Relative phase between the signal and the pump versus $\Delta\xi$ (relative input phase) at $n = 25, 50, 75$, and 210 cavity round-trips. Solid curves stand for numerical simulations from the Lugiato–Lefever equation (Eq. 4) and circles for experimental measurements. Vertical black dotted lines correspond to Eq. 1. Sim : simulations, Exp : experiments, and $\phi_s - \phi_0$ (pump–signal phase difference).

Methods

Theory and numerical simulations. We model our system with the LLE²¹ with time-dependent pump^{12,22}:

$$\frac{\partial E}{\partial z} = -\left(\frac{\alpha}{L} + i\left[\frac{\delta_0}{L} - \sum_{n=1}^{\infty} i^n \frac{\beta_n}{n!} \frac{\partial^n}{\partial t^n} - \gamma |E|^2\right]\right)E + \frac{\theta}{L}E_{in}(t) \quad (4)$$

where z is the propagation distance [$mL < z < (m+1)L$ corresponds to round-trip m], t is the time in the laboratory reference frame and $E(z, t)$ is the intra-cavity electric field. The parameters L , γ , β_1 and β_2 correspond to the cavity length, the nonlinear coefficient of the fiber, the inverse of the group velocity, and the group velocity dispersion (GVD), respectively. Note that we limited the Taylor development of the propagation constant up to the second order which is enough to capture the whole dynamics of our system operating in a relatively large dispersion regime. We checked numerically this assumption. The parameters θ and ρ define

the transmission and reflection coefficients of the coupler such that $\theta^2 + \rho^2 = 1$. The constant α accounts for the overall losses (splices, coupling, linear losses, and excess loss of the coupler) over a cavity round-trip and δ_0 is the cavity detuning³⁵. $E_{in}(t)$ describes the modulated input field, including the pump, signal, and idler fields (see Supplementary Note 1). We investigate the dynamics of this system by expanding the intra-cavity electric field into these Fourier modes^{23,24} to derive a truncated three wave model (TWM, Eq. S4 in the Supplementary Note 1) for which we calculated the steady state solution as described in Supplementary Note 1.

The LLE (Eq. 4) had been solved numerically by using a split-step Fourier procedure with a Runge–Kutta method of order 4 while the TWM (Eq. S4 in the Supplementary Note 1) by using a standard ODE solver.

Experiments. We used a continuous wave laser (laser 1 in Fig. 3) centered at 1554 nm passing through a phase modulator to generate two symmetric phase locked sidebands, the signal, and idler waves to pump the cavity. Then, an electro-optical modulator chops the wave to produce a train of 10 ns square-shaped pulses. Finally, this field is amplified and then tailored by a programmable filter (Wave-shaper), providing a fine control of the relative phase and intensity of the sidebands with respect to the carrier wave (pump). The signal/idler frequency shift is determined experimentally by launching only the pump within the cavity. After a careful adjustment of the signal/idler frequency shift in order to match with the maximum MI spontaneous gain, they are switched on to seed the process. We launched a series of bursts (210 pulses separated by the equivalent of 120 pulses) to observe the birth of MI until it reaches a stationary regime and to completely dump the cavity before the next burst. These pulses are then injected through the right port of the cavity and propagate in the anti-clockwise direction. The pump detuning (δ_0) is measured by following the approach described in ref. 38. While the pump bursts propagate in the anti-clockwise direction, the reference field propagates in the other direction along a crossed polarization state to avoid spurious cross-talk between them^{31–33}. The detection setup is inspired from the heterodyne optical time domain reflector developed in ref. 34. A multi-line local oscillator is provided by laser 2 (see Fig. 3a), which is phase locked with laser 1 with a frequency detuning of $\Delta f = 1.7$ GHz. Laser 2 is modulated by an electro-optic modulator to generate for each band to analyze (pump, signal, and idler) its own local oscillator to perform a multi-heterodyne detection system. Each beating of interest (component and its respective local oscillator component) is then filtered out by a highly selective optical filter and monitored by an oscilloscope. This way we recorded the power and phase evolutions of idler, signal, and pump waves round-trip to round-trip. The detailed experimental setup is presented in the Supplementary Note 2.

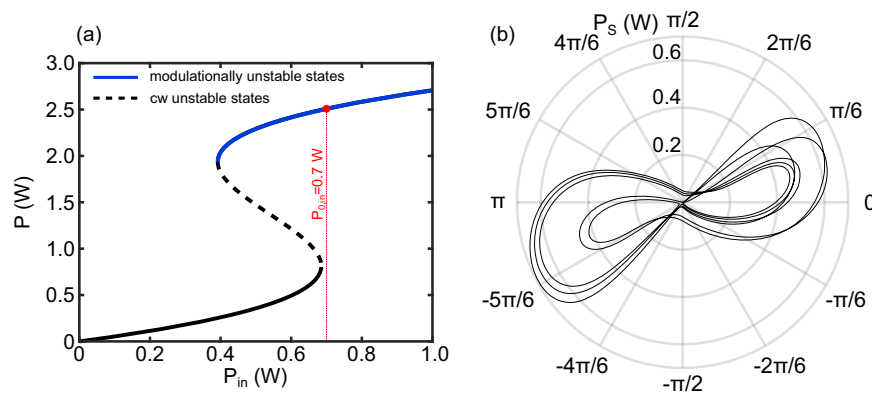


Fig. 7 Lorenz chaos in a fiber resonator: numerics. **a** Steady-state curve for $\Delta = 3$ (normalized cavity detuning). Dashed black, solid black, and solid blue curves stand for the cw unstable states, stable states, and modulatorially unstable states, respectively. **b** Trajectory of the dynamics of the system in the phase plan (P_s (signal power), $\phi_s - \phi_0$ (pump-signal signal phase difference)) for $\Delta\xi = 0$ (relative input phase) rad, corresponding to the configuration marked by the red dot in **(a)**. P stands for output power, P_{in} for input power, and CW for continuous wave.

Data availability

Most of the relevant data used in this paper are contained in the Supplementary Notes 1 and 2 while further data are available from the corresponding author upon reasonable request.

Code availability

Codes are available from the corresponding author upon reasonable request.

Received: 8 April 2021; Accepted: 18 November 2021;

Published online: 10 January 2022

References

- Zakharov, V. E. & Ostrovsky, L. A. Modulation instability: The beginning. *Phys. D: Nonlinear Phenom.* **238**, 540–548 (2009).
- Hasegawa, A. & Tappert, F. Transmission of stationary nonlinear optical pulses in dispersive dielectric fibers. I. Anomalous dispersion. *Appl. Phys. Lett.* **23**, 142–144 (2003).
- Marhic, M. E. *Fiber Optical Parametric Amplifiers, Oscillators and Related Devices* (Cambridge University Press, 2008).
- Hansryd, J., Andrekson, P. A., Westlund, M., Li, J. & Hedekvist, P.-O. Fiber-based optical parametric amplifiers and their applications. *IEEE J. Sel. Top. Quantum Electron.* **8**, 506–520 (2002).
- Andrekson, P. A. & Karlsson, M. Fiber-based phase-sensitive optical amplifiers and their applications. *Adv. Opt. Photon.* **12**, 367–428 (2020).
- Li, L. et al. All-optical regenerator of multi-channel signals. *Nat. Commun.* **8**, 1–11 (2017).
- Kippenberg, T. J., Gaeta, A. L., Lipson, M., and Gorodetsky, M. L. Dissipative Kerr solitons in optical microresonators. *Science* **361**, eaan8083 (2018).
- Pasquazi, A. et al. Micro-combs: A novel generation of optical sources. *Phys. Rep.* **729**, 1–81 (2018).
- Obrzud, E., Lecomte, S. & Herr, T. Temporal solitons in microresonators driven by optical pulses. *Nat. Photonics* **11**, 600–607 (2017).
- Obrzud, E. et al. A microphotonic astrocomb. *Nat. Photonics* **13**, 31–35 (2019).
- Brasch, V., Obrzud, E., Obrzud, E., Lecomte, S. & Herr, T. Nonlinear filtering of an optical pulse train using dissipative Kerr solitons. *Optica* **6**, 1386–1393 (2019).
- Hansson, T. & Wabnitz, S. Bichromatically pumped microresonator frequency combs. *Phys. Rev. A* **90**, 013811 (2014).
- Stekalov, D. V. & Yu, N. Generation of optical combs in a whispering gallery mode resonator from a bichromatic pump. *Phys. Rev. A* **79**, 041805 (2009).
- Bendahmane, A., Fatome, J., Finot, C., Millot, G. & Kibler, B. Selective generation of Kerr combs induced by asymmetrically phase-detuned dual pumping of a fiber ring cavity. *Opt. Lett.* **43**, 4449–4452 (2018).
- Ceolodo, D. et al. Multiple four-wave mixing and Kerr combs in a bichromatically pumped nonlinear fiber ring cavity. *Opt. Lett.* **41**, 5462–5465 (2016).
- Okawachi, Y. et al. Dual-pumped degenerate Kerr oscillator in a silicon nitride microresonator. *Opt. Lett.* **40**, 5267–5270 (2015).
- Flp, A., Krckel, C. J., Castell-Lurbe, D., Silvestre, E. & Torres-Company, V. Triply resonant coherent four-wave mixing in silicon nitride microresonators. *Opt. Lett.* **40**, 4006–4009 (2015).
- Papp, S. B., Del'Haye, P. & Diddams, S. A. Parametric seeding of a microresonator optical frequency comb. *Opt. Express* **21**, 17615–17624 (2013).
- Lin, G. et al. Spectro-temporal dynamics of Kerr combs with parametric seeding. *Appl. Opt.* **54**, 2407–2412 (2015).
- Haelterman, M., Trillo, S. & Wabnitz, S. Low dimensional modulational chaos in diffractive nonlinear cavities. *Opt. Commun.* **93**, 343–349 (1992).
- Lugiato, L. A. & Lefever, R. Spatial dissipative structures in passive optical systems. *Phys. Rev. Lett.* **58**, 2209–2211 (1987).
- Trillo, S., Wabnitz, S. & Kennedy, T. A. B. Nonlinear dynamics of dual-frequency-pumped multiwave mixing in optical fibers. *Phys. Rev. A* **50**, 1732–1747 (1994).
- Hansson, T., Modotto, D. & Wabnitz, S. Dynamics of the modulational instability in microresonator frequency combs. *Phys. Rev. A* **88**, 023819 (2013).
- Cappellini, G. & Trillo, S. Third-order three-wave mixing in single-mode fibers: exact solutions and spatial instability effects. *J. Opt. Soc. Am. B* **8**, 824–838 (1991).
- Coen, S. et al. Bistable switching induced by modulational instability in a normally dispersive all-fibre ring cavity. *J. Opt. B: Quantum Semiclass. Opt.* **1**, 36 (1999).
- Coen, S. *Passive Nonlinear Optical Fiber Resonators: Fundamentals and Applications*. Thesis, ULB (1999).
- Tabor, M. *Chaos and Integrability in Nonlinear Dynamics: An Introduction* (Wiley, 1989).
- Bar-Joseph, I., Friesem, A. A., Waarts, R. G. & Yaffe, H. H. Parametric interaction of a modulated wave in a single-mode fiber. *Opt. Lett.* **11**, 534–536 (1986).
- Tang, R. et al. Gain characteristics of a frequency nondegenerate phase-sensitive fiber-optic parametric amplifier with phase self-stabilized input. *Opt. Express* **13**, 10483–10493 (2005).
- Ippen, E. P. & Stolen, R. H. Stimulated Brillouin scattering in optical fibers. *Appl. Phys. Lett.* **21**, 539–541 (1972).
- Bessin, F., Copie, F., Conforti, M., Kudlinski, A. & Mussot, A. Modulation instability in the weak normal dispersion region of passive fiber ring cavities. *Opt. Lett.* **42**, 3730–3733 (2017).
- Copie, F., Conforti, M., Kudlinski, A., Trillo, S. & Mussot, A. Dynamics of Turing and Faraday instabilities in a longitudinally modulated fiber-ring cavity. *Opt. Lett.* **42**, 435–438 (2017).
- Bessin, F. et al. Real-time characterization of period-doubling dynamics in uniform and dispersion oscillating fiber ring cavities. *Phys. Rev. X* **9**, 041030 (2019).
- Mussot, A. et al. Fibre multi-wave mixing combs reveal the broken symmetry of Fermi–Pasta–Ulam recurrence. *Nat. Photonics* **12**, 303 (2018).
- Haelterman, M., Trillo, S. & Wabnitz, S. Additive-modulation-instability ring laser in the normal dispersion regime of a fiber. *Opt. Lett.* **17**, 745–747 (1992).
- Coulibaly, S. et al. Turbulence-induced rogue waves in Kerr resonators. *Phys. Rev. X* **9**, 011054 (2019).
- Lorenz, E. N. Deterministic nonperiodic flow. *J. Atmos. Sci.* **20**, 130–141 (1963).
- Coen, S. et al. Experimental investigation of the dynamics of a stabilized nonlinear fiber ring resonator. *J. Opt. Soc. Am. B* **15**, 2283–2293 (1998).

Acknowledgements

This work was partly supported by the Agence Nationale de la Recherche through the Equipex Fibers optiques pour les hauts flux (FLUX) through the Program Investissements d'Avenir, by the Ministry of Higher Education and Research, Hauts de France Council, and European Regional Development Fund (ERDF) through the Contrat de Projets Etat-Region (CPER Photonics for Society, P4S), HEAFISY project and I-SITE through the VERIFICO, FUHNKC and EXAT projects and H2020 Marie Skłodowska-Curie Actions (MSCA)(713694). The authors thank Dr. F. Leo, Prof. S. Coen, and Dr. F. Copie for fruitful discussions.

Author contributions

A.M., P.S., A.K., C.N., and F.B. conceived the experimental setup. C.N. and F.B. performed the experiment. F.B. and M.C. performed the numerical simulations and developed the theory. All authors contributed to analyzing the data and writing the paper.

Competing interests

The authors declare no competing interests.

Additional information

Supplementary information The online version contains supplementary material available at <https://doi.org/10.1038/s42005-021-00776-0>.

Correspondence and requests for materials should be addressed to Arnaud Mussot.

Peer review information *Communications Physics* thanks the anonymous reviewers for their contribution to the peer review of this work.

Reprints and permission information is available at <http://www.nature.com/reprints>

Publisher's note Springer Nature remains neutral with regard to jurisdictional claims in published maps and institutional affiliations.



Open Access This article is licensed under a Creative Commons Attribution 4.0 International License, which permits use, sharing, adaptation, distribution and reproduction in any medium or format, as long as you give appropriate credit to the original author(s) and the source, provide a link to the Creative Commons license, and indicate if changes were made. The images or other third party material in this article are included in the article's Creative Commons license, unless indicated otherwise in a credit line to the material. If material is not included in the article's Creative Commons license and your intended use is not permitted by statutory regulation or exceeds the permitted use, you will need to obtain permission directly from the copyright holder. To view a copy of this license, visit <http://creativecommons.org/licenses/by/4.0/>.

© The Author(s) 2022